Self-organized ion-beam synthesis of nanowires with broadband plasmonic functionality

A. Toma, D. Chiappe, C. Boragno, and F. Buatier de Mongeot[*]

Dipartimento di Fisica, Università degli Studi di Genova, and CNISM, via Dodecaneso 33, 16146 Genova, Italy
(Received 13 October 2009; revised manuscript received 2 February 2010; published 27 April 2010)

The controlled production of nanostructures endowed with well-selected shapes and reduced dimensionality represents a multidisciplinary key activity in nanotechnology. In particular, a great effort is currently oriented at the development of metal nanoparticle arrays in order to exploit the strong field-enhancement effects associated with the excitation of localized surface plasmon resonances. Here we demonstrate that ion-beam sputtering can be successfully employed to convert a polycrystalline metal film into a disconnected array of nanowires supported on a flat dielectric substrate. The nanowire arrays exhibit spectrally selective dichroic absorption due to the excitation of localized plasmon oscillations. The possibility to tailor the broadband plasmonic response has been demonstrated by finely tuning the morphological parameters of the arrays.

I. INTRODUCTION

Nanostructures endowed with controlled shapes and reduced dimensionality show interesting physical properties in several fields ranging from catalysis[1] to spintronics[2] or nanoplasmonics.[3] Within the last context, noble metal nanoparticles (NP) exhibit unique optical properties due to the excitation of collective oscillations of conduction electrons known as localized surface plasmon resonances (LSPR).[4,5] The resonance frequency of surface plasmons strongly depends on the size and shape of the NPs, thus providing an effective way for tuning their optical properties.[6,7] The strong near-field resonant coupling between light and LSPRs has been exploited for the development of molecular sensors based, e.g., on metal enhanced fluorescence,[8] surface enhanced Raman scattering,[9] or enhanced second harmonic emission.[10] The possibility to propagate the localized plasmon excitation along linear arrays of closely spaced metal NPs via near-field dipolar coupling has opened the way to intriguing developments in the field of plasmonic waveguiding and of subwavelength optoelectronics.[11] The importance of plasmonic effects has also been shown in the context of photovoltaics (PV): recent theoretical developments have highlighted the possibility to significantly enhance the photovoltaic conversion by growing a noble metal nanowire (NW) array with tailored plasmonic response near the active interface of thin film PV device.[12]

An intense research activity has thus been oriented at the development of high throughput growth methods which enable the synthesis over large areas of metal nanostructures supported on dielectric substrates.[13] Nanofabrication techniques based on self-organization are a promising alternative to the conventional lithographic or scanning probe methods, allowing low cost and maskless patterning of macroscopic surface areas. As an example in the context of plasmonic nanostructures, we can mention the use of prepatterned templates for inducing the lateral confinement of noble metal NPs.[14–18] Specifically, in[14–16] the self-organized formation of patterned templates has been demonstrated on silicon, alumina, and glass substrates recurring to defocused ion-beam sputtering (IBS). The initially flat surface is destabilized by the impinging ions and rearranges itself into nanometer-scale surface ripples oriented either parallel or perpendicular to the projection of the ion-beam direction depending on the incidence angle of the ion beam.[19,20]

Here we demonstrate that IBS patterning can be successfully employed for the *direct* self-organized synthesis of a disconnected array of NWs supported on a flat dielectric substrate, avoiding the use of prepatterned templates for the lateral confinement of the metal NPs.[21] Therefore, by employing IBS directly onto the polycrystalline metal film it is possible to fabricate NW arrays independently from the supporting material, thus extending the fabrication process to technologically relevant substrates which are not prone to develop self-organized nanostructures during ion irradiation or high-temperatures treatments.[17,18]

The so-formed NW arrays exhibit a *broadband* and tunable plasmonic response with a spectrally selective dichroic behavior due to the anisotropic excitation of LSP resonances. According to the recent theoretical predictions by Pala *et al.*[12] the tunable plasmonic response of our self-organized NW arrays renders them a low-cost candidate for the development of thin-film PV devices featuring broadband photon harvesting.

II. EXPERIMENT

Polycrystalline Au (Goodfellow, purity 99.99%) metal films were thermally deposited on soda-lime glass substrates at a rate of 6 nm/min by means of a resistively heated tungsten/alumina crucible. A calibrated quartz-crystal microbalance was used for monitoring the total thickness (150 nm) of the Au overlayer. Deposition was accomplished at room temperature within a custom designed vacuum system with a base pressure in the low 10^{-7} mbar range under unbaked conditions.

Irradiation with a defocused Ar$^+$ (5N purity) ion beam was performed *in situ* recurring to a gridded multiaperture ion source (Tectra Instruments). The patterning was done at an off-normal sputtering angle $\theta = 82°$ (measured with respect to the surface normal), an ion energy $E = 800$ eV, while the ion dose was increased from $\Theta = 2.2 \times 10^{18}$ ions cm^{-2} to $\Theta = 4.2 \times 10^{18}$ ions cm^{-2} where a well-disconnected NW array was formed. During ion irradiation the surface tempera-

ture was stabilized around $T=300$ K by means of a cooled manipulator. A biased tungsten filament, providing electrons via thermoionic emission, was placed at a distance of 10 cm with respect to the sample in order to compensate surface charging effects due to ion irradiation (when the bottom of the ripple modulation reaches the dielectric substrate exposing the glass surface).

We employed a custom-made vacuum chamber in order to make possible real-time and *in situ* monitoring of the NW array growth and end-point detection during the IBS process. The setup can acquire the optical transmittance of polarized light and detect the secondary neutral atoms sputtered from the surface with the aim of calibrating the erosion flux and detecting the end point when the metal film is carved down to the dielectric substrate (the onset of NW disconnection). For this purpose a custom secondary neutral mass spectrometer (SNMS) has been coupled by differential pumping to the IBS chamber.

The sample topography has been investigated *ex situ* by atomic force microscopy (AFM Nanosurf Mobile S, equipped with ultrasharp Si probes, PPP-NCLR-50, NanoSensors) operated in intermittent-contact mode. The optical/plasmonic properties of the NW array were investigated by means of spectroscopic transmission of polarized light in the range between 300 and 1000 nm. For this purpose we used a high-resolution solid state spectrometer (HR4000, Ocean Optics) fiber coupled to the vacuum chamber. The light source was a compensated deuterium-halogen lamp (DH-2000-BAL, Mikropak). The polarization of the incident light (normal incidence condition) was varied from transverse magnetic (TM electric field perpendicular to the NW axis) to transverse electric (TE electric field parallel to the NW axis).

III. RESULTS AND DISCUSSION

A. Morphology

An overview of the topographic evolution during Ar$^+$ irradiation at increasing fluences is reported in Fig. 1. The initial morphology is dominated by polycrystalline grains with average size peaked around 80 nm [Fig. 1(a)] while for $\Theta=2.2\times10^{18}$ ions cm^{-2} [Fig. 1(b)], $\Theta=2.7\times10^{18}$ ions cm^{-2} [Fig. 1(c)], $\Theta=3.8\times10^{18}$ ions cm^{-2} [Fig. 1(d)], and $\Theta=4.0\times10^{18}$ ions cm^{-2} [Fig. 1(e)] the surface of the metal film develops a rippled topography with ridges running parallel to the ion-beam projection in agreement with observations reported in Ref. 22. Remarkable ripple elongations, which can be comparable with the AFM image size $(2.5\times2.5\ \mu m^2)$ are found. We notice, from a statistical analysis on a significant number of AFM images that the ripple periodicity Λ remains constant around 110 nm [Fig. 1(f)].

For ion irradiation at low fluences the surface of the metal film presents a still connected rippled topography while for increasing ion doses we can expect that the bottom of the ripple modulation reaches the dielectric substrate; from this point onwards the corrugated Au film will decompose into a well-disconnected NW array. In order to achieve a direct evaluation of the residual thickness of the Au film and the
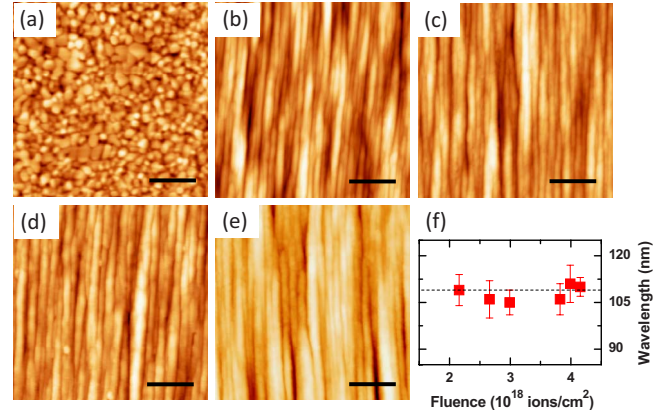

FIG. 1. (Color online) (a) Representative AFM morphology of the pristine Au film grown by physical vapor deposition (scale bar 250 nm, vertical range 12.5 nm). AFM Morphologies after Ar$^+$ irradiation at increasing fluences (scale bar 600 nm, vertical range 45 nm): (b) $\Theta=2.2\times10^{18}$ ions cm^{-2}, (c) $\Theta=2.7\times10^{18}$ ions cm^{-2}, (d) $\Theta=3.8\times10^{18}$ ions cm^{-2}, and (e) $\Theta=4.0\times10^{18}$ ions cm^{-2}. The corresponding ripple periodicity is reported in (f).

degree of NW disconnection, we have investigated by AFM sample regions where the film was mechanically removed using a micrometric tip. In this way [insets of Figs. 2(a) and 2(b)] we were able to image both the Au film and the underlying glass template on samples irradiated with increasing ion dose. We can notice that for low ion fluence $\Theta=2.2\times10^{18}$ ions cm^{-2} [Fig. 2(a)] the bottom of the Au ripples has not yet reached the glass substrate, indicated by the dashed red line. For high fluence $\Theta=4.0\times10^{18}$ ions cm^{-2} [Fig. 2(b)] the erosion of the glass substrate proceeds locally in correspondence of the Au valleys (grooves below the dashed red line). The onset of the NW disconnection has been inde-
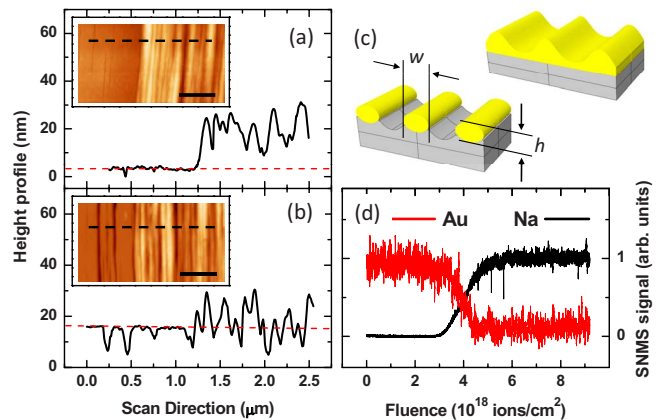

FIG. 2. (Color online) [(a)–(b)] NW formation has been investigated on samples with Au partially removed by scratch (AFM in the insets). (a) Refers to an ion dose $\Theta=2.2\times10^{18}$ ions cm^{-2} while in (b) $\Theta=4.0\times10^{18}$ ions cm^{-2}. The corresponding line profiles are shown. In the last case the erosion process is propagating into the glass substrate: the corrugated Au film is decomposed into a well-disconnected NW array. Cartoon in (c) schematically shows the surface transition from ripples to NWs. (d) The onset of the NW disconnection has been independently monitored by SNMS. Red decreasing trace (Au) refers to the metal overlayer while black increasing signal (Na) originates from the soda-lime glass substrate.
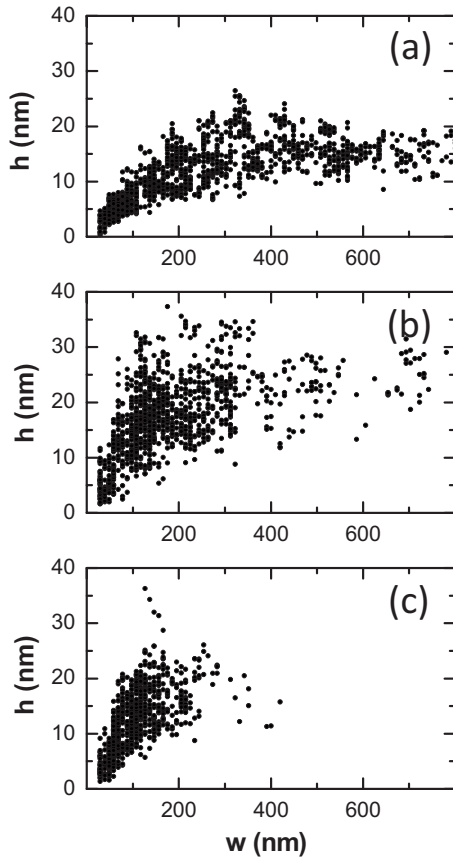
FIG. 3. Quantitative estimation of the NW cross section extracted recurring to AFM line profiles. Each point reported pertains to a specific NW cross section characterized by a pair (h, w). For $\Theta = 3.8 \times 10^{18}$ ions cm^{-2}, panel (a), a broad distribution is found, while for increasing ion doses, $\Theta = 4.0 \times 10^{18}$ ions cm^{-2} panel (b) and $\Theta = 4.2 \times 10^{18}$ ions cm^{-2} panel (c), a marked sharpening takes place.

pendently monitored *in situ* and in real time recurring to SNMS. A differentially pumped quadrupole mass spectrometer has been coupled in line-of-sight to the experimental chamber in order to collect the secondary atoms sputtered from the sample surface. In Fig. 2(d) we report, as a function of the ion dose, the evolution of the Au or Na signal respectively originating from the rippled film (red trace) or from the soda-lime glass substrate (black trace). When the metal film decomposes into a disconnected array of nanowires, the signal from the glass substrate (Na) increases while an opposite behavior is observed for the metal overalyer (Au). Increasing further the ion dose, the Na/Au signals saturate after the exhaustion of the metal film.

A quantitative estimation of the NW cross section [width w and height h, defined in Fig. 2(c)] has been extracted recurring to AFM line profiles. Each point reported in Figs. 3(a)–3(c) pertains to a specific NW cross section characterized by a pair (h, w). At the initial stages of the NW formation process, corresponding to $\Theta = 3.8 \times 10^{18}$ ions cm^{-2} [Fig. 3(a)], a broad distribution is found, while for increasing ion doses, $\Theta = 4.0 \times 10^{18}$ ions cm^{-2} [Fig. 3(b)] and $\Theta = 4.2 \times 10^{18}$ ions cm^{-2} [Fig. 3(c)] respectively, a marked sharpening takes place. Due to the intrinsic dispersion of the self-

organized pattern, the onset of the disconnection does not occur simultaneously in correspondence of each trough. In fact, as can be seen in Fig. 2(b), the deepest valleys (those which disconnect first) present a lateral separation bigger than the average periodicity of the Au ripples. At the later stage [Fig. 3(c)], when all the Au valleys have reached the substrate, the NW distribution shrinks toward lower values which are in closer connection with the original ripple periodicity.

At the intermediate stage shown in Fig. 3(b), we observe a slight increase in the NW height distribution which cannot be reconciled with a purely erosive action of the ion beam. We can attribute this to the occurrence of ion-beam-induced dewetting and coarsening of the thin Au nanostructures which are thermodynamically favored by the strong dissimilarity of the surface energy of Au and glass.[23] For higher ion doses [Fig. 3(c)] NW size reduction via ion erosion becomes finally dominant.

Summing up, we can stress that the proposed synthesis method allows to grow metallic nanowire arrays independently from the specific choice of the substrate material and without the need to prepattern it.[15] The nanofabrication process thus extends the results found on single crystal[19] and on supported polycrystalline films[22] opening the possibility to explore the functional properties of metallodielectric NPs.

B. Optical properties

The optical/plasmonic properties of the NW arrays have been verified *in situ* recurring to a solid state spectrometer fiber coupled to the vacuum chamber. The polarization of the incident light (normal incidence condition) was varied from TM to TE according to the sketch in Fig. 4(f). The spectra collected for samples irradiated with increasing ion doses, from $\Theta = 2.2 \times 10^{18}$ ions cm^{-2} to $\Theta = 4.2 \times 10^{18}$ ions cm^{-2}, are shown in Figs. 4(a)–4(e). If we measure the optical transmittance through a still connected rippled film [Fig. 4(a)] we can identify the characteristic spectral signatures measured on a flat Au metal film. The transmittance decreases toward the infrared region as expected within the simple Drude model while the typical UV transparency of a free electron metal is instead hindered by the onset of the Au interband transitions. Changing light polarization from TE to TM, no evidence of dichroic absorption is observed. The situation changes when the deepest Au valleys start to reach the substrate [Fig. 4(b) in correspondence to Na knee in the SNMS spectrum, Fig. 2(d), at $\Theta = 2.7 \times 10^{18}$ ions cm^{-2}]. The optical transmittance presents now evidence of a clear anisotropic behavior. In the case of Figs. 4(c)–4(e) (where a further decrease in height h and w was observed) the data clearly reveal the presence of a spectrally selective dichroic behavior, an indication that a well-disconnected NW array is formed. The transmittance for TE polarization still resembles the behavior of a connected Au film [Fig. 4(a)] since the NWs present elongations in the micrometer range. The transmittance for TM polarization shows a localized minimum around 770 nm [Fig. 4(c)], 720 nm [Fig. 4(d)], and 620 nm [Fig. 4(e)]. This is the typical behavior exhibited by subwavelength metal NPs sustaining a localized plasmon mode.
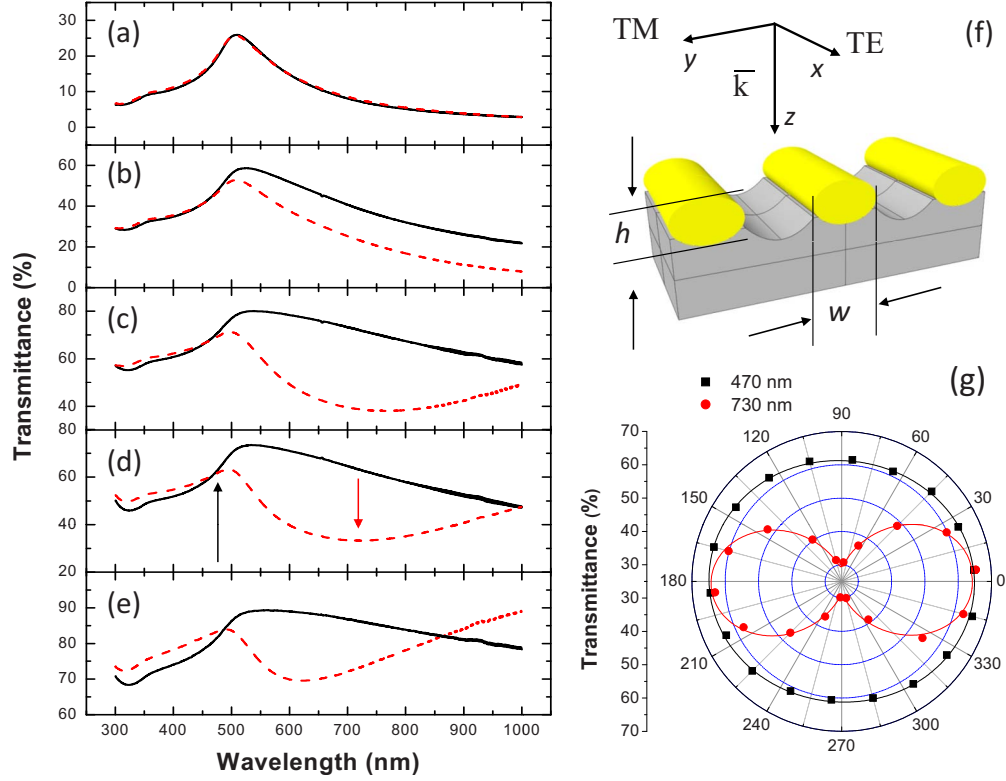
FIG. 4. (Color online) Transmission optical spectra of Au NW arrays supported on glass substrate. Panel (a) refers to the NW array of Fig. 1(b), $\Theta = 2.2 \times 10^{18}$ ions cm^{-2}, panel (b) refers to Fig. 1(c), $\Theta = 2.7 \times 10^{18}$ ions cm^{-2}, panel (c) refers to Fig. 1(d), $\Theta = 3.8 \times 10^{18}$ ions cm^{-2}, and panel (d) refers to Fig. 1(e), $\Theta = 4.0 \times 10^{18}$ ions cm^{-2}. Panel (e) corresponds to an ion dose $\Theta = 4.2 \times 10^{18}$ ions cm^{-2}. The aspect ratio is changed from $w/h = 10$ panel (c), $w/h = 6.8$ panel (d), to $w/h = 5.3$ panel (e), correspondingly the LSPR position varies from 770 to 620 nm. Red dashed lines refer to TM polarization while the black continuous ones indicate TE polarization. (f) Experimental geometry adopted for the optical investigation of the Au NWs. (g) Polar plot of optical transmittance as a function of angle between light polarization and NW axis. The data refer to the sample in panel (d) using incident light with $\lambda = 470$ and 730 nm, respectively. Continuous lines represent data fit using a $\sin^2 \theta$ function.

As already observed in Ref. 15, the NW aspect ratio dominates the optical response of the samples inducing a frequency shift in the LSPR spectral position [e.g., the resonance position changes from $\lambda = 770$ nm, Fig. 4(c), to $\lambda = 620$ nm, Fig. 4(e)]. The correlation between the morphological disconnection of the Au NWs and the onset of optical anisotropy has been confirmed by combining the analysis of the AFM scratch profile [Fig. 2(b)] to the polarized optical response. The LSPRs are excited by TM polarized light only on samples with disconnected wires [Figs. 1(c)–1(e)] while they are not excited when TE-polarized light is employed on connected Au films [Fig. 1(b)], regardless the presence of surface ripples at the vacuum-gold interface.

In addition, for increasing ion doses, we observe a progressive increase in the transmission maximum in the optical spectra due to the thinning of the metal film and to the disconnection of the metal NWs. The role of LSPR excitation in determining the anisotropic optical extinction is further confirmed in Fig. 4(g) by comparing the amplitude modulation of the transmitted signal. The latter is plotted as a function of the orientation θ between the light polarization and the NW axis, for two different light wavelengths [arrows in Fig. 4(d)], respectively, tuned at the plasmon resonance ($\lambda = 730$-nm-red trace) and detuned from it ($\lambda = 470$-nm-black trace). For $\lambda = 730$ nm the optical transmittance presents a strongly anisotropic modulation due to the LSPR excitation while for $\lambda = 470$ nm the modulation becomes negligible and a quasi-isotropic response is found. We can quantitatively describe the angular dependence of the transmitted intensity (at a selected wavelength λ) recurring to

$$I(\lambda, \theta) = I_0(\lambda) - I_1(\lambda)\sin^n \theta, \qquad (1)$$

where $I_0(\lambda)$ is the intensity transmitted for TE polarization, similar to the behavior encountered in a continuous film, while $I_1(\lambda)\sin^n \theta$ takes into account the additional extinction due to the angular-dependent plasmon excitation. A remarkably good agreement is found between Eq. (1) [continuous lines in Fig. 4(g)] and the experimental data for $n=2$, corresponding to the above mentioned $\sin^2 \theta$ relation. This is not surprising since the LSPR is excited by the perpendicular component (TM polarization) of the incoming light, proportional to $|\boldsymbol{E}|^2 \sin^2 \theta$.

The experimental optical spectra have been compared to calculations within the quasistatic approximation (as already discussed in Ref. 15) under the assumption that the separation between two adjacent wires is large enough to avoid strong interparticle coupling. In the case of samples in Figs. 4(c)–4(e), the average interwire spacings are in the range 60–110 nm; we can thus expect, as experimentally verified in

Ref. 24, that the interparticle interaction plays a negligible role on the spectral position of the LSP resonance.

The NWs are modeled as polarizable ellipsoids with their principal axis l oriented along the ripple ridges direction. The polarizability α_n along one of the axis directions assumes the following expression:[4]

$$\alpha_n(\omega) = \frac{V_{NW}}{4\pi} \frac{\varepsilon(\omega) - \varepsilon_m}{\varepsilon_m + L_n[\varepsilon(\omega) - \varepsilon_m]} \quad \text{for} \quad n = x, y, z, \quad (2)$$

where V_{NW} is the nanowire volume, $\varepsilon(\omega)$ and ε_m denote the dielectric function of the NWs and the host medium, respectively. In order to describe the effect of the surrounding medium on the optical spectra of metal NWs, an effective dielectric constant

$$\varepsilon_m = (1 + n_S^2)/2 \quad (3)$$

is assumed as embedding the particle completely (n_S is the refractive index of the glass substrate).[25]

The polarizabilty associated with the n axis depends on geometrical parameters through the depolarization factors L_n.[4–7,16] Here we extend the previous result to the case of a very slender ellipsoid ($l \gg w \geq h$ and $L_x \neq L_y \neq L_z$) which appears to be more appropriate for the present NW geometry (more details can be found in the Appendix). The optical extinction can be calculated recurring to Eq. (2). For a light beam polarized along the n direction parallel to one of the main axes of the NW array, the absorption and scattering efficiencies are given by[4,6,7]

$$Q_{abs}^n = \frac{2\pi V_{NW} \varepsilon_m^{3/2}}{\lambda A_{NW} L_n^2} \frac{\varepsilon_2}{\left| \varepsilon(\omega) + \dfrac{1 - L_n}{L_n} \varepsilon_m \right|^2}, \quad (4)$$

$$Q_{sca}^n = \frac{\pi^2 V_{NW}^2 \varepsilon_m^2}{\lambda^4 A_{NW} L_n^2} \left| \frac{\varepsilon(\omega) - \varepsilon_m}{\varepsilon(\omega) + \dfrac{1 - L_n}{L_n} \varepsilon_m} \right|^2 F_n, \quad (5)$$

where λ is the wavelength of the incident light, ε_2 the imaginary part of the NW dielectric function $\varepsilon(\omega)$ and A_{NW} represents the effective NW cross section. Equation (5) for the scattering efficiency contains a polarization-dependent form factor F_n coming out from the Rayleigh-Gans approximation[4] as described in more detail in the Appendix.

The position of the LSPR can be derived minimizing the denominator of Eq. (2) and is thus completely determined by the NW geometrical parameters. The measured polarization-dependent transmission spectra can be reproduced within this model, which allows to correlate the broadening of the extinction peak with the large distribution of the NW cross sections (inhomogeneous broadening). Using the distribution of the NW cross section—the pairs (h, w) reported in Figs. 3(a)–3(c)—and the principal axis length $l = 3000$ nm ($l \gg w > h$), directly extracted from the AFM topographies, we were able to calculate the depolarization factors L_n of a size-dispersed NW array and thus to assess the importance of inhomogeneous broadening. In Figs. 5(a)–5(c) we plot the simulated absorption efficiency Q_{abs} for the experimentally determined distribution of NW cross sections [(h, w) for the
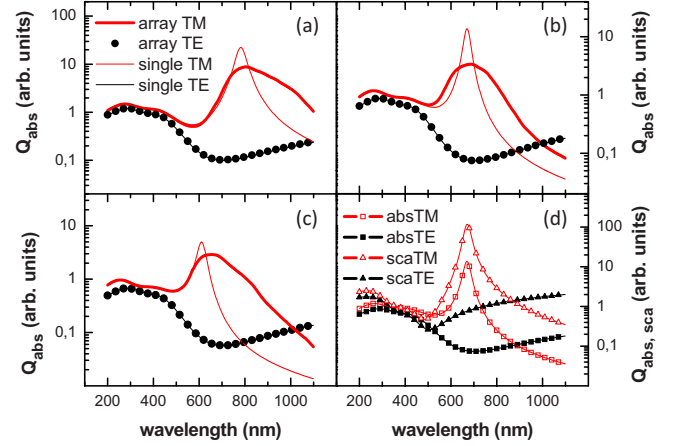

FIG. 5. (Color online) [(a)–(c)] Calculated absorption efficiency for the samples in Figs. 4(c)–4(e). Panel (a) corresponds to $\Theta = 3.8 \times 10^{18}$ ions cm^{-2}, panels (b)–(d) $\Theta = 4.0 \times 10^{18}$ ions cm^{-2}, and panel (c) $\Theta = 4.2 \times 10^{18}$ ions cm^{-2}. The curves clearly show the importance of inhomogeneous broadening (thick line and filled dots) in comparison to the case of a monodisperse array of NWs (thin lines). (d) Comparison between absorption (open and filled squares) and scattering (open and filled triangles) efficiencies, evaluated according to Eqs. (4) and (5) for the monodispersed NW array already plotted in panel (b).

samples of Figs. 4(c)–4(e)], and we compare it with a monodisperse array of NWs of identical size (corresponding to the average value of w/h). As expected, the plasmonic properties of the NW array depend in a direct way on their morphology: the intrinsic broadband response derives from the size distribution in the NW cross section (typical of the self-organized processes) and allows to excite the LPSR over a relatively wide range of frequencies, a positive feature in view of broadband photovoltaic applications.[12] Moreover, since absorption and scattering efficiencies, Eqs. (4) and (5), respectively scale with V_{NW} and V_{NW}^2, we can expect that for our NWs the scattering efficiency dominates over absorption.[5] As an example, in Fig. 5(d) we compare the scattering and absorption efficiencies, evaluated according to Eqs. (4) and (5) for the monodispersed NW array already plotted in Fig. 5(b). For TM polarization Q_{sca} is one order of magnitude higher than Q_{abs}, and the spectral line shape is almost equivalent in both the cases, being dominated by the LSP resonance. Also for TE polarization, the scattering dominates over the absorption efficiency and thus determines the trend of the extinction spectrum.

In Figs. 6(a)–6(c) we systematically investigated how the calculated optical scattering efficiency is affected by the experimental distribution of NW aspect ratios. Also in this case the importance of inhomogeneous broadening is evident. Moreover, since scattering is the dominant term in the extinction efficiency, a better agreement with the experimental transmission spectra is found both for TE and TM polarization.

In Fig. 6(d) we plot the calculated wavelength of the LSPR which has been derived minimizing the denominator of Eq. (2), as a function of w/h, and we compare it with the experimental values extracted from the optical spectra shown before [Figs. 4(c)–4(e)]. We also include the data points
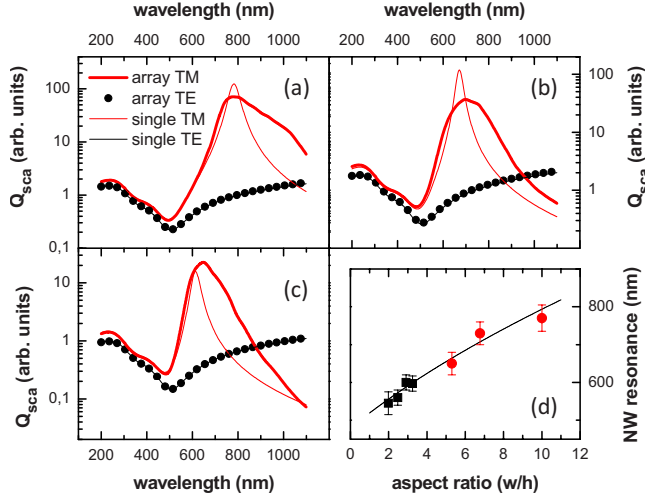
FIG. 6. (Color online) [(a)–(c)] Calculated scattering efficiency for the samples in Figs. 4(c)–4(e). Panel (a) corresponds to Θ $=3.8\times10^{18}$ ions cm^{-2}, panel (b) $\Theta=4.0\times10^{18}$ ions cm^{-2}, and panel (c) $\Theta=4.2\times10^{18}$ ions cm^{-2}. The curves show again the importance of inhomogeneous broadening (thick line and filled dots) in comparison to the monodispersed case (thin lines). Moreover, since scattering is the dominant term in the extinction efficiency, a better agreement with the experimental transmission spectra is found. (d) Experimental positions for the TM resonance mode, as a function of the aspect ratio w/h (red circles). The black continuous curve represents the calculated LSPR position. The black squares refer to deposition on prepatterned templates (Ref. 15).

(black squares) discussed in Ref. 15 in order to show that direct IBS patterning of polycrystalline films can extend the results obtained on prepatterned templates,[14–18] shifting the LPSR spectral position toward the near-infrared region.

IV. CONCLUSIONS

In conclusion, we described a self-organized approach for the physical synthesis of laterally ordered arrays of metallic NWs supported on dielectric materials. The method, does not require the prepatterning of the dielectric template and could thus be generalized to substrates of a technologically relevant material such as, e.g., flexible and transparent polymers. The formation of a disconnected array of NWs allows the excitation of localized surface plasmon resonances. The morphological anisotropy of the NWs affects their optical transmittance which presents a strong dichroism due to the selective excitation of localized plasmons for orthogonal light polarization. The possibility to tailor the broadband plasmonic properties of the NWs in the visible spectral range has been demonstrated by changing the morphological parameters of the arrays, making them a low-cost candidate for the development of thin film PV devices featuring broadband photon harvesting.

APPENDIX: AUXILIARY CALCULATIONS

A model based on the quasistatic approximation was here employed to describe the NW arrays fabricated by direct IBS irradiation. The NWs were modeled as polarizable ellipsoid with their principal axis l oriented along the ripple ridges direction [x axis in Fig. 4(f)]. The dipolar polarizability α_n has been described in Eq. (2) by introducing depolarization factors L_n which take into account the geometry of the NPs.[4–7,16] In particular, for the case of very slender ellipsoid ($l \gg w \geq h$) we obtain:

$$L_x = \frac{wh}{l^2}\left[\ln\left(\frac{4l}{w+h}\right)-1\right] \tag{A1}$$

for TE polarization and

$$L_y = \frac{h}{w+h}-\frac{wh}{2l^2}\ln\left(\frac{4l}{w+h}\right)+\frac{wh(3w+h)}{4l^2(w+h)} \tag{A2}$$

for TM polarization.

The dielectric function of the metal NWs was analytically described recurring to the model proposed by Etchegoin *et al.* in Refs. 26 and 27 appropriately modified in order to take into account for size and interface effects. The frequency collision Γ was changed to $\Gamma=\Gamma_0+v_f/r$, where $\Gamma_0=v_f/R$ represents the frequency collision in the bulk material, R the electron mean-free path in Au metal, v_f the corresponding Fermi velocity and $r=l/2$ or $w/2$, respectively, for TE or TM polarization.

The scattering efficiency Q_{sca} was stated in Eq. (5) and differs from expressions used in Refs. 6 and 7 for the presence of a polarization-dependent form factor F_n coming out from the Rayleigh-Gans approximation for the scattering matrix elements.[4] For the geometry encountered in the present work F_n assumes the following expression:

$$F_x = \int_0^{2\pi}\int_0^{\pi} G^2(u)\sin^3\vartheta\, d\vartheta\, d\varphi \tag{A3}$$

and

$$F_y = \int_0^{2\pi}\int_0^{\pi}(\cos^2\varphi+\cos^2\vartheta\,\sin^2\varphi)G^2(u)\sin\vartheta\, d\vartheta\, d\varphi \tag{A4}$$

for an incoming light beam polarized along TE or TM, respectively. The function $G(u)$ has the form: $G(u)$ $=3/u^3(\sin u-u\cos u)$, where

$$u = \frac{2\pi l}{\lambda}\sqrt{\cos^2\vartheta+\left(\frac{w}{l}\right)^2(\sin^2\vartheta-2\sin\vartheta\cos\varphi+1)} \tag{A5}$$

being ϑ and φ the spherical coordinate system coupled with the NW main axis.

*Corresponding author; buatier@fisica.unige.it

[1] F. Buatier de Mongeot, A. Toma, A. Molle, S. Lizzit, L. Petaccia, and A. Baraldi, Phys. Rev. Lett. **97**, 056103 (2006).

[2] P. Gambardella, S. Rusponi, M. Veronese, S. S. Dhesi, C. Grazioli, A. Dallmeyer, I. Cabria, R. Zeller, P. H. Dederichs, K. Kern, C. Carbone, and H. Brune, Science **300**, 1130 (2003).

[3] E. Ozbay, Science **311**, 189 (2006).

[4] C. F. Bohren and D. R. Huffman, *Absorption and Scattering of Light by Small Particles* (Wiley, New York, 1998).

[5] U. Kreibig and M. Vollmer, *Optical Properties of Metal Clusters* (Springer-Verlag, Berlin, 1995).

[6] O. Muskens, D. Christofilos, N. Del Fatti, and F. Vallée, J. Opt. A, Pure Appl. Opt. **8**, S264 (2006).

[7] E. Stefan Kooij and B. Poelsema, Phys. Chem. Chem. Phys. **8**, 3349 (2006).

[8] J. N. Anker, W. P. Hall, O. Lyandres, N. C. Shah, J. Zhao, and R. P. Van Duyne, Nature Mater. **7**, 442 (2008).

[9] X. Qian, X. H. Peng, D. O. Ansari, Q. Yin-Goen, G. Z. Chen, D. M. Shin, L. Yang, A. N. Young, M. D. Wang, and S. Nie, Nat. Biotechnol. **26**, 83 (2008).

[10] A. Belardini, M. C. Larciprete, M. Centini, E. Fazio, C. Sibilia, M. Bertolotti, A. Toma, D. Chiappe, and F. Buatier de Mongeot, Opt. Express **17**, 3603 (2009).

[11] S. Lal, S. Link, and N. J. Halas, Nat. Photonics **1**, 641 (2007).

[12] R. A. Pala, J. White, E. Barnard, J. Liu, and M. L. Brongersma, Adv. Mater. **21**, 3504 (2009).

[13] J. V. Barth, G. Costantini, and K. Kern, Nature (London) **437**, 671 (2005).

[14] T. W. H. Oates, A. Keller, S. Facsko, and A. Mücklich, Plasmonics **2**, 47 (2007).

[15] A. Toma, D. Chiappe, D. Massabò, C. Boragno, and F. Buatier de Mongeot, Appl. Phys. Lett. **93**, 163104 (2008).

[16] S. Camelio, D. Babonneau, D. Lantiat, L. Simonot, and F. Pailloux, Phys. Rev. B **80**, 155434 (2009).

[17] S. Camelio, D. Babonneau, D. Lantiat, and L. Simonot, EPL **79**, 47002 (2007).

[18] E. Fort, C. Ricolleau, and J. Sau-Pueyo, Nano Lett. **3**, 65 (2003).

[19] U. Valbusa, C. Boragno, and F. Buatier de Mongeot, J. Phys.: Condens. Matter **14**, 8153 (2002).

[20] W. L. Chan and E. Chason, J. Appl. Phys. **101**, 121301 (2007).

[21] F. Buatier de Mongeot, C. Boragno, U. Valbusa, D. Chiappe, and A. Toma, PCT Patent Publication No.: WO/2009/109939 (11.09.2009).

[22] A. Toma, D. Chiappe, B. Šetina Batič, M. Godec, M. Jenko, and F. Buatier de Mongeot, Phys. Rev. B **78**, 153406 (2008).

[23] J. Lee, M. Nakamoto, and T. Tanaka, J. Mater. Sci. **40**, 2167 (2005).

[24] S. A. Maier, M. L. Brongersma, P. G. Kik, and H. A. Atwater, Phys. Rev. B **65**, 193408 (2002).

[25] F. Neubrech, T. Kolb, R. Lovrincic, G. Fahsold, A. Pucci, J. Aizpurua, T. W. Cornelius, M. E. Toimil-Molares, R. Neumann, and S. Karim, Appl. Phys. Lett. **89**, 253104 (2006).

[26] P. G. Etchegoin, E. C. Le Ru, and M. Meyer, J. Chem. Phys. **125**, 164705 (2006).

[27] P. G. Etchegoin, E. C. Le Ru, and M. Meyer, J. Chem. Phys. **127**, 189901 (2007).